

On the symmetry of the phonon landscape across the duality boundary of twisted kagomes lattices

Stefano Gonella*

*Department of Civil, Environmental, and Geo- Engineering
University of Minnesota, Minneapolis, MN 55455, USA*

In this letter, we investigate the symmetry of the phonon landscape of twisted kagome lattices across their duality boundary. The study is inspired by recent work by Fruchart et al. [Nature, 577, 2020], who specialized the notion of duality to the mechanistic problem of kagome lattices and linked it to the existence of duality transformations between configurations that are symmetrically located across a critical transition point in configuration space. Our first goal is to elucidate how the existence of matching phonon spectra between dual configurations manifest in terms of observable wavefield characteristics. To this end, we explore the possibility to aggregate dual kagome configurations into bi-domain lattices that are geometrically heterogeneous but retain a mechanically homogeneous response. Our second objective is to extend the analysis to structural lattices of beams, which are representative of realistic cellular metamaterials. We show that, in this case, the symmetry of the phonon landscape across the duality boundary is broken, implying that the conditions for dual behavior do not merely depend on the geometry, but also on the dominant mechanisms of the cell, suggesting a dichotomy between geometric and functional duality.

Kagome lattices are a special family of two-dimensional periodic structures whose unit cell consists of two triangular elements (solid or hollow) connected at one vertex. The most prominent example is the regular kagome lattice, in which two equilateral triangles are rotated by 180° with respect to each other. Over the past two decades, kagome lattices have received growing attention in the literature on periodic structures and metamaterials, with a variety of studies addressing their mechanical properties^{1–5} and their wave propagation characteristics^{6–9}. Kagome lattices have also been studied as viable models to approximate the behavior of biological materials such as cartilage¹⁰, as well as effective configurations for lattice-based medical implants¹¹. Twisted kagome structures represent a variation upon the classical kagome paradigm, whereby the triangles are rotated by arbitrary angles, leading to dramatic changes in equivalent mechanical properties and phononic characteristics¹², including a switch between bulk and shear as the dominant stiffness-providing mechanism.

Many peculiar properties of kagome lattices stem from the fact that they belong to the family of so-called Maxwell lattices^{13,14}, i.e., lattices that contain an equal number of degrees of freedom and constraints in the bulk and, for this reason, are on the verge of mechanical instability^{15–17}. Recently, a spur of interest has surrounded the discovery of phenomena that are rooted in the topology of kagome architectures. Specifically, topological kagome lattices, which can be obtained from the regular kagome geometry by deforming (or deforming and twisting) the triangles, have been shown to display topological polarization¹⁸, which can be tuned by controlling the twist and stretch of the cell¹⁹. The polarization is

responsible for the existence of floppy edges at which deformation can be focused, yielding edge modes that decay into the bulk. In dynamics, it has been shown that the floppy edges support edge-confined phonons at finite frequencies^{20–22} and the polarization endows the lattices with asymmetric wave transport behavior.

Recently, Fruchart et al. revisited the mechanics of twisted kagome lattices putting forth the notion of duality²³. Duality can be interpreted as a behavioral symmetry in the parameter space of the twist angle, whereby configurations that are equidistant (in configuration space) from a critical transition angle feature identical phonon band diagrams. In²³, this property is linked to the existence of a precise duality transformation between pairs of configurations on either side of the critical point. This letter proposes a reflection on this powerful result and on the implications of duality for wave manipulation in cellular metamaterials. We first focus on lattices of rods, in which ideal lattice conditions are preserved, and we elucidate the practical manifestation of duality in the spatio-temporal characteristics of propagating wave packets. We then explore the transportability of the framework to structural lattices of beams connected by internal clamps. This case mimics the realistic conditions that are observed in cellular metamaterials obtained using fabrication techniques such as cutting or additive manufacturing, thus capturing conditions that are of utmost relevance for engineering applications.

The unit cell of a twisted kagome lattice, shown in Fig. 1(a), consists of two arbitrarily rotated equilateral triangles (of side length L). In this study, the hollow triangles are taken to be either trusses of rods connected by hinges, or frames of beams joined by internal clamps. In the former case, the lattice bonds support only tension/compression and the perfect hinges allow free rotation of the rods, thus approximating ideal lattice conditions (although, here, the mass is not lumped at the lat-

* sgonella@umn.edu

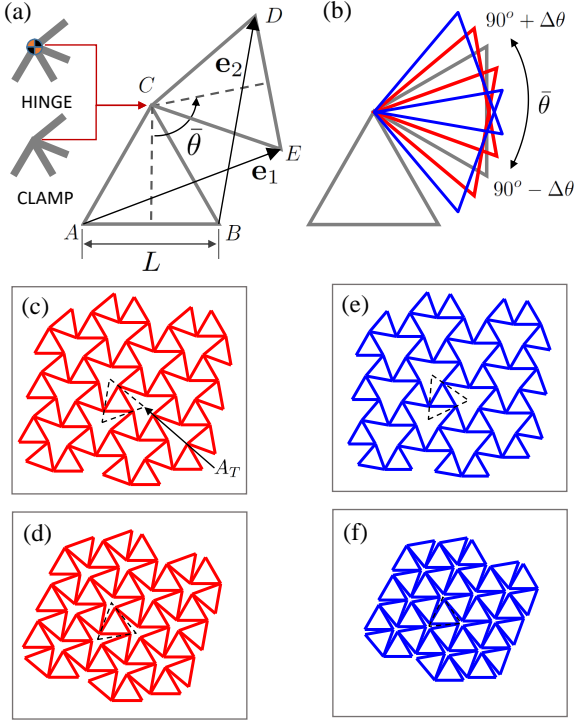


FIG. 1. (a) Geometry of the twisted kagome lattice unit cell, showing primitive vectors and choice of hinge or clamp conditions. (b) Twisted kagome lattice family parameterized in terms of the twist angle $\bar{\theta}$. (c)-(d) Dual pair with $\bar{\theta} = 105^\circ$ and $\theta = 75^\circ$. (e)-(f) Dual pair with $\theta = 110^\circ$ and $\bar{\theta} = 70^\circ$.

tice sites). In the latter case, the lattice bonds support bending deformation and the clamps offer infinite resistance to the relative rotation of the beams. The geometry can be conveniently parameterized in terms of the twist angle θ , defined here as the angle by which the top triangle is rotated about hinge point C , such that $\theta = 0^\circ$ yields two overlapping triangles and $\bar{\theta} = 180^\circ$ returns the regular kagome cell. The primitive vectors are expressed as $\mathbf{e}_1 = [L/2 + L \sin(\bar{\theta} - 30^\circ)] \mathbf{i}_1 + [\sqrt{3}L/2 - L \cos(\bar{\theta} - 30^\circ)] \mathbf{i}_2$ and $\mathbf{e}_2 = [-L/2 + L \cos(\bar{\theta} - 60^\circ)] \mathbf{i}_1 + [\sqrt{3}L/2 + L \sin(\bar{\theta} - 60^\circ)] \mathbf{i}_2$, with $\mathbf{i}_1, \mathbf{i}_2$ Cartesian unit vectors. With reference to Fig. 1(b), we refer to configuration pairs $90^\circ \pm \Delta\theta$ (symmetrically located across the 90° reference configuration in $\bar{\theta}$ -space) as *dual pairs*. Two sets of dual pairs are denoted in red and blue and the resulting lattices, color-coded accordingly, are shown in Fig. 1.(c)-(d) and (e)-(f).

We proceed to compute the phonon band diagrams for $\bar{\theta} \in [70^\circ 110^\circ]$. The results, shown in Fig. 2, are color-coded to highlight all the dual pairs. The normalized frequency Ω is obtained as $\Omega = \omega/\omega_{0R}$, where $\omega_{0R} = \pi/L\sqrt{E/\rho}$ is the first natural frequency of a rod of length L , Young's modulus E and density ρ . It is easy to conclude that dual cells have identical phonon structures, retrieving a picture of duality analogous to that presented in²³ (in which, note, the lattices have lumped masses, leading to slightly different branch morphology).

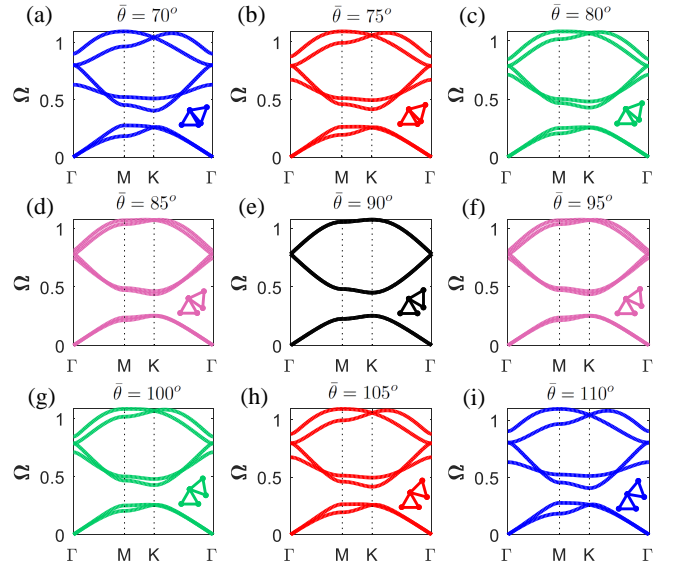


FIG. 2. Band diagrams for lattices of rods connected by hinges for $\bar{\theta} \in [70^\circ 110^\circ]$, color-coded to highlight the dual pairs, for which *matching* phonon spectra are obtained.

It is important at this stage to clarify how a matching phonon landscape between dual configurations translates into dimensional wavefield descriptors. In Fig. 2, the non-dimensional wavevector is sampled along the $\Gamma\text{MK}\Gamma$ path in reciprocal space. Since the reciprocal lattices vary with $\bar{\theta}$, the dimensional wavevector $\mathbf{k} = k_x \mathbf{i}_1 + k_y \mathbf{i}_2$ in Cartesian coordinates changes between configurations. As a result, two corresponding points in the band diagrams of dual configurations denote plane waves with different physical wavelengths and propagation directions. Accordingly, the phase velocity vector $\mathbf{c}^p = \omega \mathbf{k}/\|\mathbf{k}\| = c_x^p \mathbf{i}_1 + c_y^p \mathbf{i}_2$ varies in magnitude and orientation and the directivity patterns of the dispersion surfaces are rotated between configurations (details in SI).

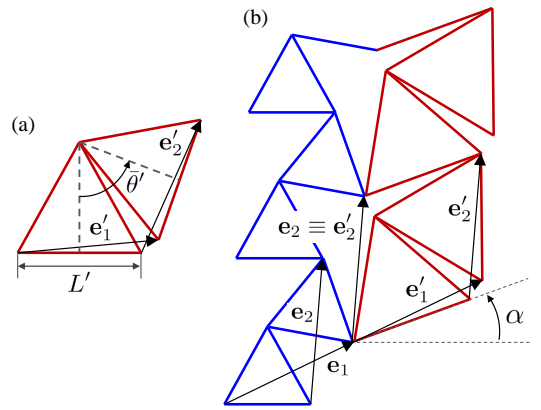


FIG. 3. (a) Unit cell of lattice 2 with $\bar{\theta}' = 70^\circ$, to be stitched to its $\bar{\theta} = 110^\circ$ dual. (b) Stitching strategy showing compatibility constraints necessary to obtain a matching interface.

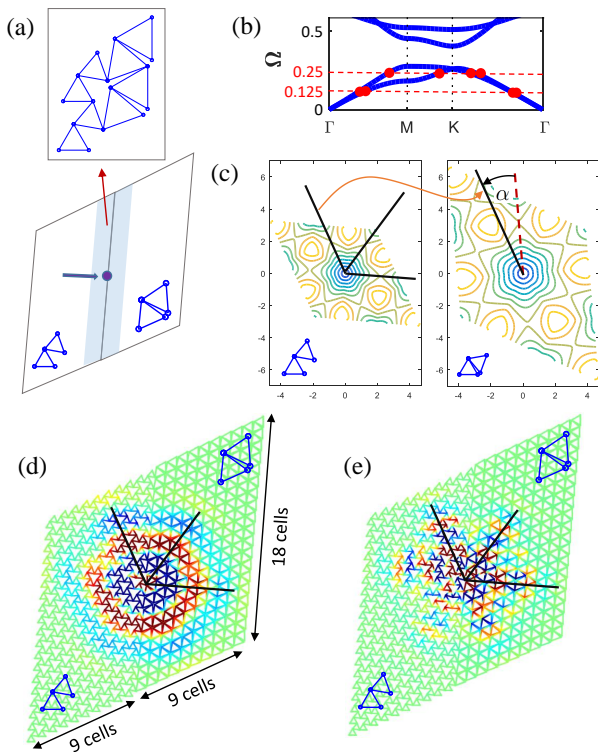


FIG. 4. (a) Schematic of lattice with $\bar{\theta} = 110^\circ$ and $\bar{\theta}' = 70^\circ$ subdomains, properly stitched through geometric and material compensation. (b) Detail of band diagram, with highlighted frequencies of excitation. (c) I mode iso-frequency contours for $\bar{\theta} = 110^\circ$ and $\bar{\theta} = 70^\circ$, showing inherent directivity mismatch between dual configurations. (d) and (e) Snapshots of wavefields excited by tone-bursts centered at $\Omega = 0.125$ and $\Omega = 0.25$, respectively. The wavefields show *matching* propagation characteristics in the two subdomains.

An effective way to realize phonon duality conditions within these constraints is to construct a lattice composed of two subdomains meeting at an interface. This task allows us to envision the design of metamaterials that are simultaneously geometrically heterogeneous and mechanically, or functionally, homogeneous. The construction strategy is depicted in Fig. 3 adopting $\bar{\theta} = 110^\circ$ for lattice 1 and $\bar{\theta}' = 70^\circ$ for lattice 2 (quantities pertaining to lattice 2 are labeled by (\prime)). It can be seen that, in order to have a matching interface, lattice 2 must feature a larger characteristic size L' and rotate by an angle α with respect to lattice 1. The primitive vectors \mathbf{e}'_1 and \mathbf{e}'_2 are obtained by replacing L with L' and $\bar{\theta}$ with $\bar{\theta}'$ in the expressions for lattice 1. We recognize from Fig. 3(b) that, at the interface, \mathbf{e}_2 and its counterpart \mathbf{e}'_2 must match (upon rotation by α). Therefore, to find L' , it is sufficient to enforce $\|\mathbf{e}_2\| = \|\mathbf{e}'_2\|$ and solve for L' , and α is precisely the angle by which \mathbf{e}'_2 must rotate to overlap with \mathbf{e}_2 , hence $\alpha = \cos^{-1}\left(\frac{\mathbf{e}_2 \cdot \mathbf{e}'_2}{\|\mathbf{e}_2\| \|\mathbf{e}'_2\|}\right)$. Moreover, since the frequencies in the phonon spectra are normalized by ω_{0R} , which follows the jump from L to L' , the phonon

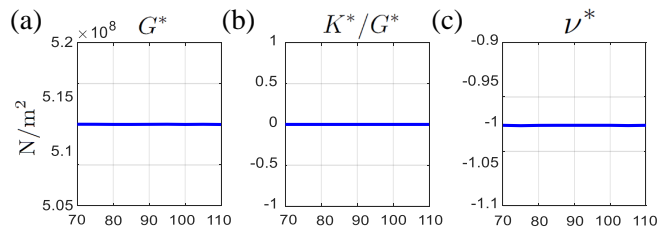


FIG. 5. Effective moduli of lattices of rods vs. $\bar{\theta}$. (a) Effective shear modulus G^* , assuming $L = 1$ m, $\beta = 1/15$ and material properties of Aluminum: Young's modulus $E = 70 \cdot 10^9$ N/m², Poisson's ratio $\nu = 0.33$, density $\rho = 2700$ Kg/m³. (b) Ratio between effective bulk modulus K^* and effective shear modulus G^* . (c) Effective Poisson's ratio ν^* .

correspondence is compromised across the interface. In order to compensate for this jump and preserve duality conditions across the interface, we need to correct the properties of lattice 2. Since $\omega_{0R} \propto 1/L\sqrt{E/\rho}$, this can be achieved by choosing the material properties of lattice 2 such that $(E/\rho)'/(E/\rho) = (L'/L)^2$.

We consider now a domain comprising two dual subdomains, as shown in Fig. 4(a). A force excitation, in the form of a 5-cycle tone burst, is applied at the center of the domain perpendicular to the interface. In Fig. 4(b) we show how the selected frequencies intersect the matching band diagrams of the dual configurations. At $\Omega = 0.125$, we expect nearly-isotropic propagation while, at $\Omega = 0.25$, the behavior is highly directional. In Fig. 4(c) we compare the iso-frequency contour lines for the dual lattices (assuming non-rotated cells of size L for both). We confirm that the inherent directivity landscape is rotated between the two by precisely α . This directional mismatch is automatically compensated by the rotation operation performed while stitching the lattices. Two snapshots of the wavefields are shown in Fig. 4(d) and (e). Both wavefields are found to have matching characteristics across the interface. This result shows that we can design geometrically heterogeneous, yet functionally homogeneous domains by stitching dual kagome configurations. The strategy, however, requires a multi-material design with specific tailoring requirements.

From the band diagrams, we can inversely estimate the effective elastic moduli. First, we determine the effective density $\rho^* = \rho\bar{\rho}$, where ρ is the material density and $\bar{\rho}$ is the relative density, obtained from the geometry of a half cell by dividing the area occupied by solid material by the total “foot print” area A_T (shown in Fig. 1(c)). Here, $\bar{\rho} = 3Lh/A_T$, where $h = \beta L$ and β is the rod's slenderness ratio. We then determine numerically the phase velocities c_S^p and c_L^p of the acoustic modes in the long-wavelength limit ($\|\mathbf{k}\| \rightarrow 0$). By comparing c_S^p and c_L^p along ΓM and ΓK , it is easy to verify that the long-wavelength behavior is isotropic for all $\bar{\theta}$. Finally, the effective shear modulus G^* and bulk modulus K^* are computed from the relations for linear homogeneous and isotropic media: $c_S^p = \sqrt{G^*/\rho^*}$ and

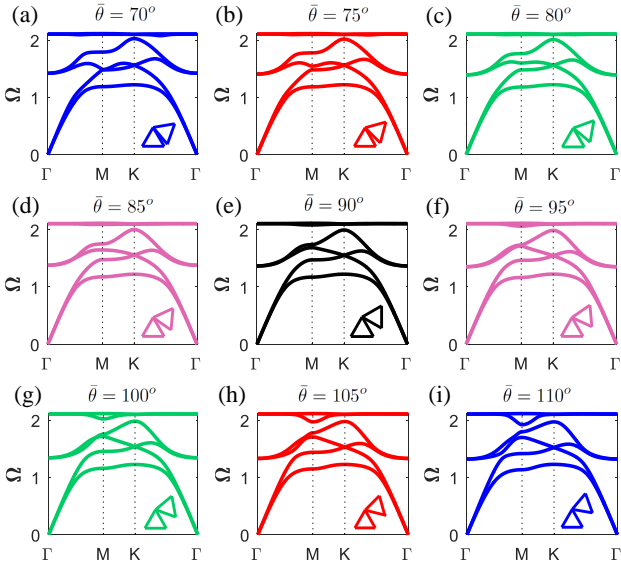


FIG. 6. Band diagrams for lattices of beams for $\bar{\theta} \in [70^\circ 110^\circ]$, color-coded to highlight the dual pairs. In this case, the phonon spectra of dual pairs are *different*.

$c_L^p = \sqrt{(K^* + G^*)/\rho^*}$. $G^*(\bar{\theta})$, plotted in Fig. 5(a) for the material selection given in the caption, is found to be constant for all $\bar{\theta}$. As inferable from the plot of K^*/G^* in Fig. 5(b), the procedure yields negligible bulk modulus values (here, the methodology, which is sensitive to inaccuracies in the inference of c_S^p and c_L^p , yields small enough values that can be effectively interpreted as $K^* \approx 0$). The effective Poisson's ratio ν^* is found from the relation $\nu^* = (K^* + G^*)/(K^* - G^*)$ for 2D plane-stress²⁴. We see in Fig. 5(c) that ν^* approaches -1 (deep auxetic behavior) for all θ . These results are consistent with the theoretical properties for ideal twisted kagome lattices¹².

We now switch our focus to lattices of beams. We study the same configurations used for the rod case, but the lattice bonds are now modeled as Timoshenko beams (4 beam elements per bond). The Timoshenko model is robust against a wide spectrum of the slenderness ratios $\beta = h/L$, capturing with high degree of accuracy even the behavior of thick beams (above $\beta = 1/5$) for which the shear deformability is not negligible⁶. However, since our configurations feature extremely re-entrant angles, excessively large β values are unrealistic, as the clamps would morph into platelets that would challenge the validity of a beam model. Therefore, in this study, we will focus on slender beams ($\beta = 1/10$ in our calculations).

The band diagrams for $\bar{\theta} \in [70^\circ 110^\circ]$ are shown in Fig. 6. The frequency is normalized by the first natural frequency of a simply-supported beam of length L $\omega_{0B} = \pi^2/L^2 \sqrt{EI/\rho A}$, where A and I are the cross-sectional area and second moment of area. Interestingly, the band diagrams of dual pairs are no longer identical, with differences that grow when we move away from the critical angle. In the SI, we show that these differences become more pronounced as β increases. The equivalent

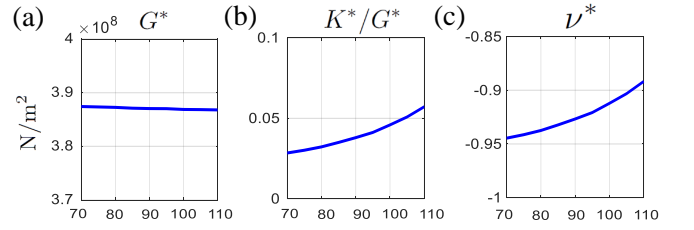


FIG. 7. Effective moduli of lattices of beams vs. $\bar{\theta}$. (a) Effective shear modulus G^* . (b) Ratio between effective bulk modulus K^* and G^* . (c) Effective Poisson's ratio ν^* .

elastic moduli are shown in Fig. 7. We see that bending mechanisms and clamp-like connections cause appreciable deviations from the properties of ideal lattices. While G^* is still almost constant for all $\bar{\theta}$, K^* , while remaining significantly smaller than G^* , is no longer negligible. Similarly, ν^* deviates from -1, albeit remaining in the deep auxetic regime. Moreover, the property landscape is no longer symmetric about the duality boundary.

We now revisit the domain with $\bar{\theta} = 110^\circ$ and $\bar{\theta}' = 70^\circ$ dual pairs as a lattice of beams. Since $\omega_{0B} \propto 1/L\sqrt{E/\rho}\beta$ and we keep β constant across the interface, it is again sufficient to select the material properties of lattice 2 such that $(E/\rho)'/(E/\rho) = (L'/L)^2$ to establish identical spectral conditions across the interface. In Fig. 8(a) we compare the band diagrams for $\bar{\theta} = 110^\circ$ and $\bar{\theta} = 70^\circ$. In Figs. 8(b)-(c), we show snapshots of the wavefields obtained for the excitation frequencies indicated in Fig. 8(a). We observe that the waves now propagate in the two subdomains with different directionality and different levels of dispersion despite the geometric duality of the subdomains.

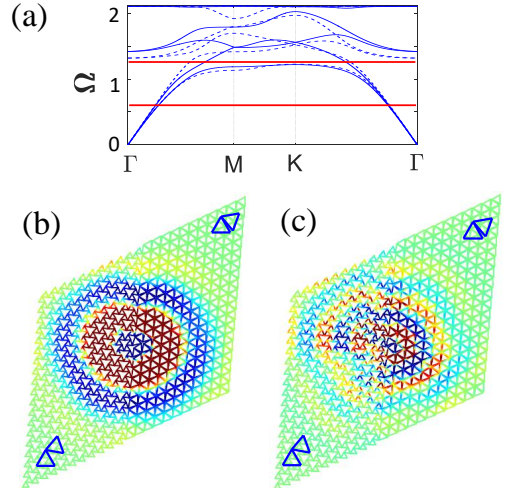


FIG. 8. (a) Band diagrams for lattices of beams with $\bar{\theta} = 110^\circ$ and $\bar{\theta} = 70^\circ$, superimposed with excitation frequencies highlighted. (b)-(c) Snapshots of wavefields excited by frequencies indicated in (a). The wavefields feature different directionality and dispersion characteristics in the two subdomains.

A powerful way to assess the potentials of lattices with non-uniform geometry but uniform dynamic characteristics is presented in Fig. 9. We consider a 6×6 lattice constrained around its perimeter. We compare a lattice of rods, shown in Fig. 9(a), where the perimeter nodes are hinged, against a lattice of beams, shown in Fig. 9(b), where the nodes are clamped. For each scenario, we compare two cases. In case 1, $\bar{\theta} = 110^\circ$ everywhere. In case 2, we stitch two strips of dual configurations (with $\bar{\theta} = 110^\circ$ and $\bar{\theta}' = 70^\circ$). The natural frequencies computed for the two cases are superimposed as blue circles and red squares. We see that, with rods, the natural frequencies of the single- and bi-domain lattices match (up to small deviations attributable to the small domain size, depart-

ing from the infinite lattice conditions of Bloch analysis). In contrast, with beams, the curves present a significant mismatch that grows with the mode index. This result confirms that, for ideal connections, dual lattices can be treated as dynamically equivalent solids and seamlessly coupled. This is not the case for structural lattices.

In conclusion, we have shown that dual configurations with matching phonon spectra can be leveraged to design metamaterials that are geometrically heterogeneous and functionally homogeneous. This effect is, however, diluted when we depart from ideal lattice conditions.

This work is supported by NSF (Grant EFRI-1741618).

- ¹ S. Hyun and S. Torquato, *Journal of Materials Research* **17**, 137144 (2002).
- ² N. A. Fleck and X. Qiu, *Journal of the Mechanics and Physics of Solids* **55**, 562 (2007).
- ³ D. Simons and N. Fleck, *Journal of Applied Mechanics* **75**, 051011 (2008).
- ⁴ Y. Zhang, X. Qiu, and D. Fang, *International Journal of Solids and Structures* **45**, 3751 (2008).
- ⁵ S. Arabnejad and D. Pasini, *International Journal of Mechanical Sciences* **77**, 249 (2013).
- ⁶ A. Phani, J. Woodhouse, and N. Fleck, *J. Acoust. Soc. Am.* **119**, 1995 (2006).
- ⁷ M. Schaeffer and M. Ruzzene, *Journal of Applied Physics* **117**, 194903 (2015).
- ⁸ E. Riva, D. E. Quadrelli, G. Cazzulani, and F. Braghin, *Journal of Applied Physics* **124**, 164903 (2018).
- ⁹ H. Chen, H. Nassar, A. N. Norris, G. K. Hu, and G. L. Huang, *Phys. Rev. B* **98**, 094302 (2018).
- ¹⁰ J. L. Silverberg, A. R. Barrett, M. Das, P. B. Petersen, L. J. Bonassar, and I. Cohen, *Biophysical Journal* **107**, 17211730 (2014).
- ¹¹ S. A. Khanoki and D. Pasini, *Journal of the Mechanical Behavior of Biomedical Materials* **22**, 65 (2013).
- ¹² K. Sun, A. Souslov, X. Mao, and T. Lubensky, *Proceedings of the National Academy of Sciences* **109** (2012).
- ¹³ J. C. Maxwell, *Philos. Mag.* **27**, 294 (1864).
- ¹⁴ C. Calladine, *International Journal of Solids and Structures* **14**, 161 (1978).
- ¹⁵ T. Lubensky, C. Kane, X. Mao, A. Souslov, and K. Sun, *Reports on Progress in Physics* **78**, 073901 (2015).
- ¹⁶ A. Souslov, A. J. Liu, and T. C. Lubensky, *Physical Review Letters* **103**, 205503 (2009).
- ¹⁷ X. Mao and T. C. Lubensky, *Physical Review E* **83**, 011111 (2011).
- ¹⁸ C. Kane and T. Lubensky, *Nature Physics* **10**, 39 (2014).
- ¹⁹ D. Z. Rocklin, S. Zhou, K. Sun, and X. Mao, *Nature communications* **8** (2017).
- ²⁰ J. Ma, D. Zhou, K. Sun, X. Mao, and S. Gonella, *Physical Review Letters* **121**, 094301 (2018).
- ²¹ O. Stenull and T. C. Lubensky, *Physical Review Letters* **122**, 248002 (2019).
- ²² D. Zhou, J. Ma, K. Sun, S. Gonella, and X. Mao, *Phys. Rev. B* **101**, 104106 (2020).
- ²³ M. Fruchart, Y. Zhou, and V. Vitelli, *Nature* **577**, 636 (2020).
- ²⁴ J. W. Eischen and S. Torquato, *Journal of Applied Physics* **74**, 159 (1993).

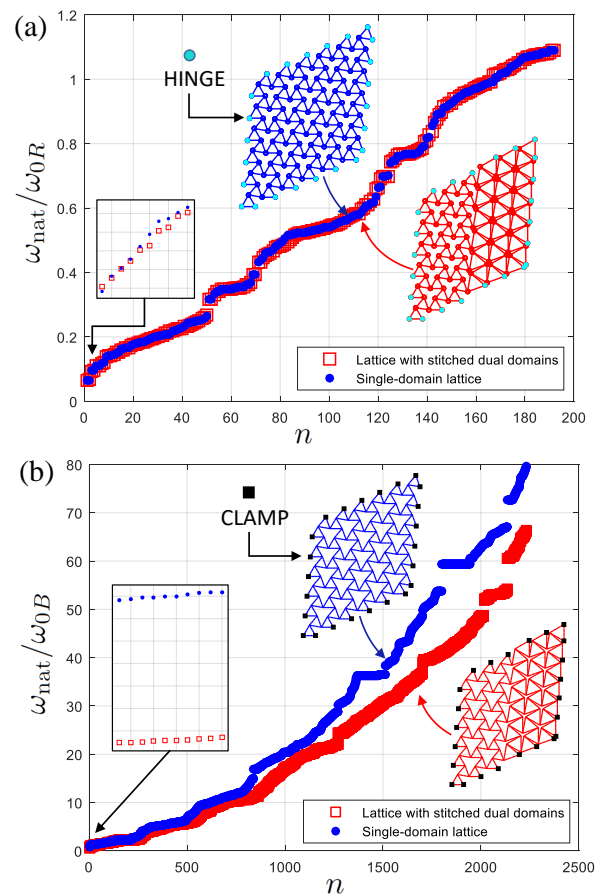


FIG. 9. Comparison of natural frequencies between single-domain lattice and bi-domain lattice featuring stitched dual configurations. (a) Lattice of rods: the natural frequencies match perfectly. (b) Lattice of beams: strong deviations are observed between the two cases.

I. SUPPLEMENTAL INFORMATION

I.1. Wavelength and directivity mismatch between dual configurations

In Fig. 10, we compare the iso-frequency contour lines for the I mode for lattices of rods connected by hinges, for $\bar{\theta} \in [70^\circ 110^\circ]$. If we compare dual configurations (e.g., (a) vs. (i)), we note that the magnitude of the wavevectors (and, consequently, wavelengths) and the directivity landscape are different, despite matching band diagrams.

I.2. Effect of the slenderness ratio on the phonon duality for lattices of beams

In Figs 11 and 12, we plot the band diagrams for lattices of beams (with $\bar{\theta} \in [70^\circ 110^\circ]$) for slenderness ratio $\beta = 1/15$ and $\beta = 1/5$, respectively. We see that the differences between the phonon bands of dual configurations become more pronounced as β increases, especially at low frequencies. The more we deviate from ideal lattice conditions (perfect hinges), the more the symmetry across the duality boundary is diluted.

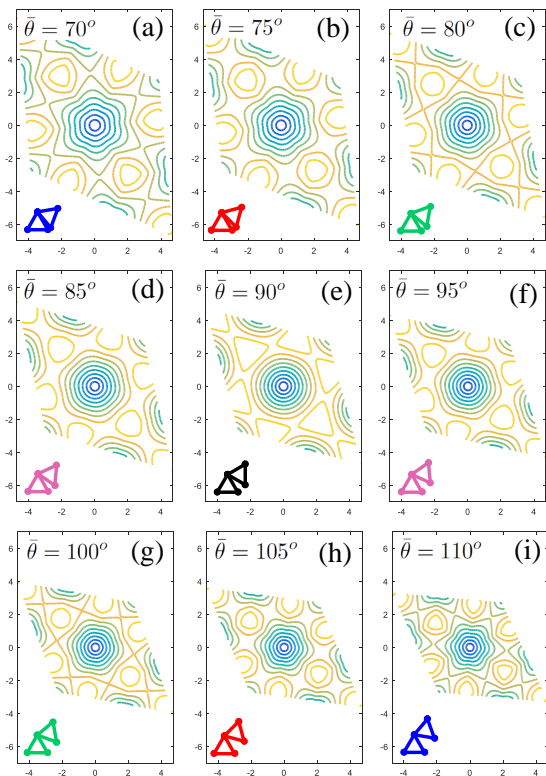


FIG. 10. Iso-frequency contour lines for the I mode for lattice of rods connected by hinges for $\bar{\theta} \in [70^\circ 110^\circ]$.

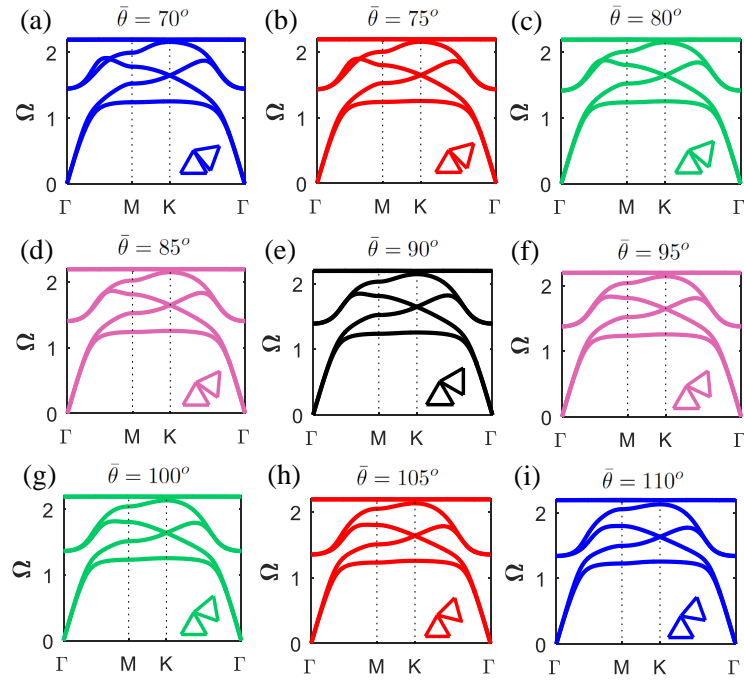


FIG. 11. Band diagram for lattice of beams with slenderness ratio $\beta = 1/15$, for $\bar{\theta} \in [70^\circ 110^\circ]$.

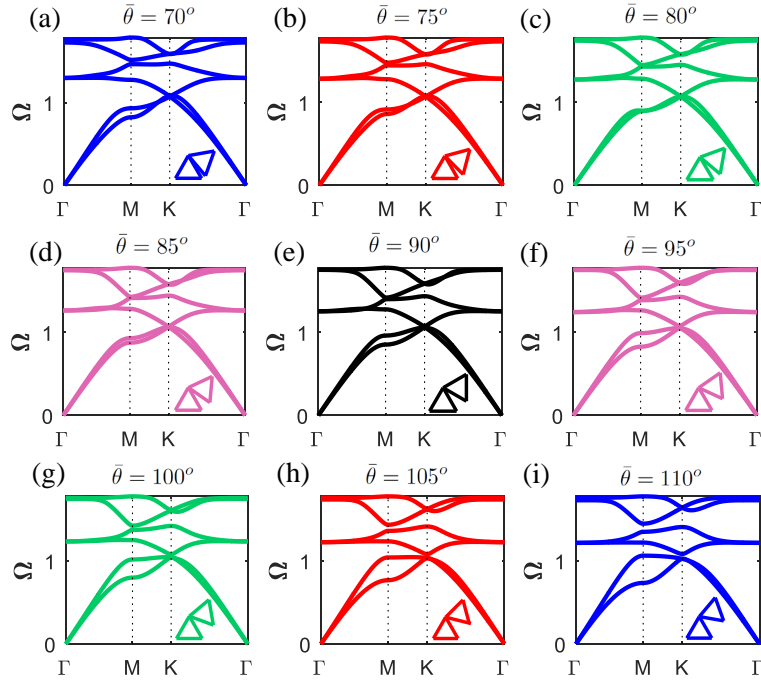


FIG. 12. Band diagram for lattice of beams with slenderness ratio $\beta = 1/5$, for $\bar{\theta} \in [70^\circ 110^\circ]$.